Geophysical Journal International

Geophys. J. Int. (2010) **182,** 923–932 doi: 10.1111/j.1365-246X.2010.04643.x

Empirically determined finite frequency sensitivity kernels for surface waves

Fan-Chi Lin and Michael H. Ritzwoller

Center for Imaging the Earth's Interior, Department of Physics, University of Colorado at Boulder, Boulder, CO 80309-0390*, USA. E-mail: linf@colorado.edu*

Accepted 2010 April 26. Received 2010 April 22; in original form 2010 January 28

SUMMARY

We demonstrate a method for the empirical construction of 2-D surface wave phase traveltime finite frequency sensitivity kernels by using phase traveltime measurements obtained across a large dense seismic array. The method exploits the virtual source and reciprocity properties of the ambient noise cross-correlation method. The adjoint method is used to construct the sensitivity kernels, where phase traveltime measurements for an event (an earthquake or a virtual ambient noise source at one receiver) determine the forward wave propagation and a virtual ambient noise source at a second receiver gives the adjoint wave propagation. The interference of the forward and adjoint waves is then used to derive the empirical kernel. Examples of station–station and earthquake–station empirical finite frequency kernels within the western United States based on ambient noise and earthquake phase traveltime measurements across USArray stations are shown to illustrate the structural effects on the observed empirical sensitivity kernels. We show that a hybrid kernel constructed from the empirical kernel and the kernel for a reference model can be used to compute traveltimes accurate to second order in model perturbations for an earth-like model. A synthetic test demonstrates the application of such hybrid kernels to predict surface wave phase traveltimes.

Key words: Surface waves and free oscillations; Seismic tomography; Wave propagation.

1 INTRODUCTION

Seismic waves with non-infinite (finite) frequencies are sensitive to earth structures away from the geometrical ray. This finite frequency effect is particularly important for surface wave tomography because of the relatively long periods, wavelengths and path lengths involved, especially in teleseismic applications (Yoshizawa & Kennett 2002; Zhou *et al.* 2004; Yang & Forsyth 2006). Surface wave tomography is often based on ray theory with either straight (e.g. Barmin *et al.* 2001) or bent (refracted) rays (Lin *et al.* 2009), and in some cases regularization is introduced to mimic off-ray sensitivity (e.g. Barmin *et al.* 2001) or approximate analytical sensitivity kernels are applied (e.g. Ritzwoller *et al.* 2002; Levshin *et al.* 2005). Surface wave tomography methods based on accurate finite frequency kernels potentially can improve resolution compared to ray theory and resolve subwavelength structures. Whether such tomographic methods based on analytical finite frequency kernels derived from a 1-D earth model are better than methods using *ad hoc* kernels or even ray theory remains under debate (e.g. Yoshikawa & Kennett 2002; van der Hilst & de Hoop 2005; Montelli *et al.* 2006; Trampert & Spetzler 2006).

With advances in computational power and numerical methodology, in particular with the development of the adjoint method (Tromp *et al.* 2005), increasingly accurate numerical sensitivity kernels based on more realistic 2-D and 3-D reference models have begun to emerge. The use of these numerical sensitivity kernels in tomographic inversions has also begun to appear (e.g. Peter *et al.* 2007; Tape *et al.* 2009). The method remains computationally imposing, however, particularly when the data set and number of model parameters are large.

The emergence of large, density seismic arrays, such as the EarthScope/USArrary Transportable Array, stimulated the development of a number of new surface wave tomography methods that track wave fronts and move beyond straight-ray tomography (e.g. Langston & Liang 2008; Pollitz 2008), including eikonal tomography (Lin *et al.* 2009). In eikonal tomography, for each period the phase traveltime map $\tau_s(\boldsymbol{x})$ is measured on a fine spatial grid from an event by fitting a minimum curvature surface across all available phase traveltime measurements within the region. The gradient of the phase traveltime map is then used to solve for local wave properties such as the direction of propagation and phase velocity. Although Lin *et al.* 2009 focused mainly on waves emitted by virtual sources in the ambient noise cross-correlation application, the same method can be applied to earthquake data. Whether meaningful amplitude information and the full Green's function (Tanimoto 2008) can be extracted from ambient noise cross correlations is still under investigation, however amplitude information $A_s(\boldsymbol{x})$ can, in principle, be determined for an earthquake event with amplitude measurements across the region.

In this study, we extend the construction of the empirically determined phase traveltime maps to include 2-D empirical (non-analytical and non-numerical) phase traveltime sensitivity kernels

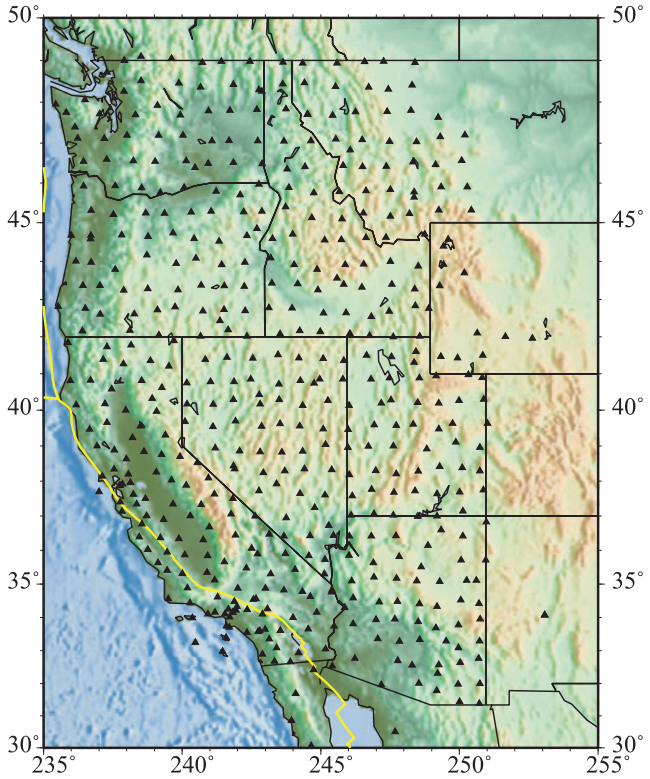

Figure 1. The USArray Transportable Array stations used in this study.

for surface waves across a large array where, in essence, the real Earth acts as the reference model. We follow the basic idea of the adjoint method, however instead of performing numerical simulations we use the observed phase traveltime maps to obtain the necessary information about wave propagation. In particular, we utilize the virtual source property of the ambient noise cross-correlation measurements to obtain information about wave propagation due to an impulsive force at one station location to mimic the adjoint simulation in the numerical method. The western United States covered by EarthScope USArray stations (Fig. 1) is used to demonstrate this method. Empirical sensitivity kernels for both ambient noise and telesiesmic earthquakes across USArray are presented and the effects of regional phase speed variations (Fig. 2) are illustrated. Although examples are presented only for Rayleigh waves at periods of 20, 30 and 40 s, in principle the method is extendable to shorter and longer periods and to Love waves when reliable traveltime maps are available.

Traditional finite frequency tomography is based on a linear relationship between traveltimes and model perturbations, which breaks down when the model perturbation is large and when off great-circle propagation effects are important. The empirical kernels provide a direct measure of the strength of this non-linearity and, therefore, provide a test of existing methods. In addition, we demonstrate in Section 4 that the empirical kernels can be used in conjunction with kernels constructed from a reference model to improve the accuracy of traveltime predictions. We present pilot simulations to exemplify this effect. The application of empirical kernels in tomographic inversions will move beyond both geometrical ray theory and single scattering theory in a computationally efficient way. This application is, however, beyond the scope of this paper and will be the subject of a future contribution.

2 THE THEORETICAL BACKGROUND

A detailed theoretical derivation of the adjoint method to construct a 2-D phase traveltime sensitivity kernel for surface waves by approximating the surface wave as a membrane wave was presented by Peter *et al.* (2007). For a fixed event location $\boldsymbol{x}_e$, the authors showed that the phase traveltime perturbation $\delta\tau(\boldsymbol{x}_r)$ measured by the waveform cross-correlation method at the receiver location $\boldsymbol{x}_r$ due to local phase speed perturbations $\delta c(\boldsymbol{x})$ can be linked through a surface integral

$$\delta\tau(x_r) = \int_\Omega K(\mathbf{x}, \mathbf{x}_r)\, \tau_0 \frac{\delta c(\mathbf{x})}{c_0(\mathbf{x})} \mathrm{d}\mathbf{x}, \tag{1}$$

and the sensitivity kernel $K(\mathbf{x}, \mathbf{x}_r)$ at field position $\boldsymbol{x}$ can be expressed as

$$K(\mathbf{x}, \mathbf{x}_r) = -\frac{2}{\tau_0 c_0^2(\mathbf{x})} \int_0^T s^\dagger(\mathbf{x}, \mathbf{x}_r, T-t)\, \partial_t^2 s(\mathbf{x}, t)\, \mathrm{d}t, \tag{2}$$

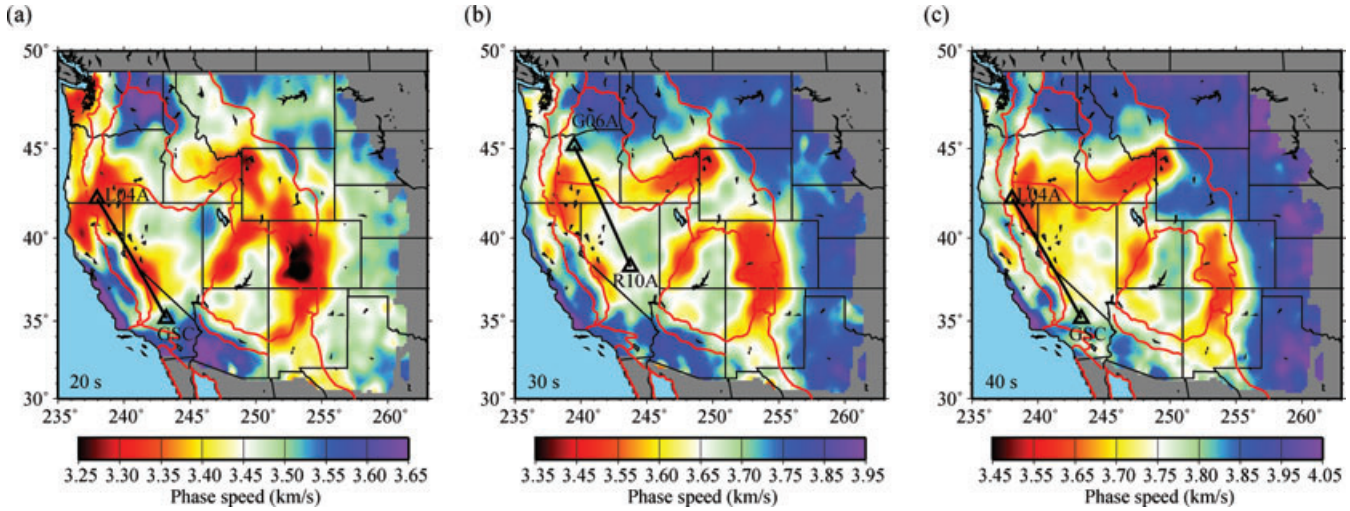

Figure 2. The (a) 20 s, (b) 30 s and (c) 40 s period Rayleigh-wave phase speed maps determined from all available vertical–vertical component ambient noise cross correlations between 2004 October and 2009 August across USArray. The eikonal tomography method (Lin *et al.* 2009) is used to construct these maps. The stations used in Figs 3 and 4 to construct the station–station empirical kernels are also shown.

where τ_0 is the reference phase traveltime between the event and the receiver, c_0 is the phase speed for the reference model, T is the duration of the seismogram, $s^\dagger$ is the adjoint wavefield and s is the forward wavefield. The adjoint wavefield $s^\dagger$ is the wavefield emitted by an adjoint source $f^\dagger$ at the receiver location

$$f^\dagger(\mathbf{x}, t) = \frac{1}{N} w\,(T-t)\,\partial_t s\,(\mathbf{x}_r, T-t)\,\delta(\mathbf{x}-\mathbf{x}_r), \tag{3}$$

where N is a normalization factor defined by

$$N = \int_0^T w(t) s\,(\mathbf{x}_r, t)\,\partial_t^2 s\,(\mathbf{x}_r, t)\,\mathrm{d}t, \tag{4}$$

and $w(t)$ denotes the cross-correlation time window for the phase traveltime measurement.

For a phase traveltime at an instantaneous frequency, we simplify the equation for the forward wavefield by assuming a sinusoidal source such that

$$s(\mathbf{x}, t) = A_s(\mathbf{x}) \cos\{\omega[t - \tau_s(\mathbf{x})]\}, \tag{5}$$

where $A_s(\mathbf{x})$ and $\tau_s(\mathbf{x})$ are the forward wavefield's amplitude and phase traveltime at each location and ω is the angular frequency. We note that in existing adjoint tomography (e.g. Peter *et al.* 2007) only the phase traveltime $\tau_s(\mathbf{x}_r)$ at the receiver $\mathbf{x}_r$ is measured empirically. In contrast, we also determine the phase traveltime $\tau_s(\mathbf{x})$ empirically for other locations $\boldsymbol{x}$ across the array.

Substituting eq. (5) into eq. (3), the adjoint source $f^\dagger$ can be rewritten as

$$f^\dagger(\mathbf{x}, t) = \frac{\omega}{N} w\,(T-t)\,A_s\,(\mathbf{x}_r) \sin\{\omega[T-t-\tau_s\,(\mathbf{x}_r)]\}\,\delta(\mathbf{x}-\mathbf{x}_r). \tag{6}$$

By assuming an infinitely wide time sampling window in which $w(t) = 1$ for all t, the adjoint wavefield $s^\dagger$ can then be expressed as

$$s^\dagger(\mathbf{x}, \mathbf{x}_r, t) = \frac{-\omega}{N} A_s(\mathbf{x}_r) A_{s^\dagger}(\mathbf{x}, \mathbf{x}_r) \sin\{\omega[-T + t + \tau_s(\mathbf{x}_r) - \tau_{s^\dagger}(\mathbf{x}, \mathbf{x}_r)]\}, \tag{7}$$

$$s^\dagger(\mathbf{x}, \mathbf{x}_r, T-t) = \frac{\omega}{N} A_s(\mathbf{x}_r)\,A_{s^\dagger}(\mathbf{x}, \mathbf{x}_r) \cos\left\{\omega[-t + \tau_s\,(\mathbf{x}_r) - \tau_{s^\dagger}\,(\mathbf{x}, \mathbf{x}_r)] + \frac{\pi}{2}\right\}, \tag{8}$$

where $A_{s^\dagger}(\mathbf{x}, \mathbf{x}_r)$ and $\tau_{s^\dagger}(\mathbf{x}, \mathbf{x}_r)$ represent the adjoint wavefield amplitude and phase traveltime due to an impulsive force with unit amplitude at the receiver location. Substituting eq. (8) into eq. (2) and assuming the duration of the seismogram is sufficiently large, the finite frequency sensitivity kernel for an instantaneous frequency ω can be expressed as

$$K_{\mathrm{in}}(\mathbf{x}, \mathbf{x}_r, \omega) = \frac{-2\omega A_{s^\dagger}\,(\mathbf{x}, \mathbf{x}_r)}{\tau_0 c_0^2\,(\mathbf{x})} \left(\frac{A_s\,(\mathbf{x})}{A_s\,(\mathbf{x}_r)}\right) \cos\left\{\omega[\tau_s\,(\mathbf{x}_r) - \tau_{s^\dagger}\,(\mathbf{x}, \mathbf{x}_r) - \tau_s\,(\mathbf{x})] + \frac{\pi}{2}\right\}. \tag{9}$$

For a constant speed reference model $c(\mathbf{x}) = c_0'$ under the far field approximation, $A_{s^\dagger}(\mathbf{x}, \mathbf{x}_r)$, $\tau_{s^\dagger}(\mathbf{x}, \mathbf{x}_r)$, $A_s(\mathbf{x})$ and $\tau_s(\mathbf{x})$ can be derived analytically from the Green's function of the Helmholtz equation (e.g. Yoshizawa & Kennett 2005) as

$$A_{s^\dagger}(\mathbf{x}, \mathbf{x}_r) = \sqrt{\frac{1}{8\pi k\,|\mathbf{x}-\mathbf{x}_r|}}, \tag{10a}$$

$$\tau_{s^\dagger}\,(\mathbf{x}, \mathbf{x}_r) = \frac{|\mathbf{x}-\mathbf{x}_r|}{c_0'} + \frac{\pi}{4\omega}, \tag{10b}$$

$$A_s\,(\mathbf{x}) = \sqrt{\frac{1}{8\pi k\,|\mathbf{x}-\mathbf{x}_e|}}, \tag{10c}$$

$$\tau_s\,(\mathbf{x}) = \frac{|\mathbf{x}-\mathbf{x}_e|}{c_0'} + \frac{\pi}{4\omega}, \tag{10d}$$

where $k = \frac{\omega}{c_0'}$ is the wavenumber and $\boldsymbol{x}_e$ is the event location. Substituting these expressions into eq. (9) and letting $\tau_0 = \frac{|\mathbf{x}_r-\mathbf{x}_e|}{c_0'}$, the analytical kernel $K_{in}^a(\mathbf{x}, \mathbf{x}_r, \omega)$ for instantaneous frequency ω based on a 1-D earth model can be expressed as

$$K_{in}^a\,(\mathbf{x}, \mathbf{x}_r, \omega) = \frac{-2\omega}{|\mathbf{x}_r-\mathbf{x}_e|\,c_0'} \left(\sqrt{\frac{|\mathbf{x}_r-\mathbf{x}_e|}{8\pi k\,|\mathbf{x}-\mathbf{x}_e|\,|\mathbf{x}-\mathbf{x}_r|}}\right) \times \cos\left[k\,(|\mathbf{x}_r-\mathbf{x}_e| - |\mathbf{x}-\mathbf{x}_r| - |\mathbf{x}-\mathbf{x}_e|) + \frac{\pi}{4}\right], \tag{11}$$

which is similar to the 2-D analytical phase kernel derived by Zhou *et al.* (2004) based on a 1-D earth model. Note that for the kernel notation, the superscript is '*e*' (empirical) or '*a*' (analytical) and the subscript is 'in' (instantaneous) or 'fb' (finite bandwidth).

Starting from eq. (9), the sensitivity kernel for a surface wave between a seismic event and a receiver at an instantaneous frequency at an arbitrary location $\boldsymbol{x}$ can be determined empirically with knowledge of the forward amplitude $A_s(\mathbf{x})$, forward phase traveltime $\tau_s(\mathbf{x})$, adjoint amplitude $A_{s^\dagger}(\mathbf{x}, \mathbf{x}_r)$, adjoint phase traveltime $\tau_{s^\dagger}(\mathbf{x}, \mathbf{x}_r)$, the local phase speed $c_0(\mathbf{x})$ and the forward wavefield's amplitude $A_s(\mathbf{x}_r)$ and phase traveltime $\tau_s(\mathbf{x}_r)$ measured at the receiver location. Among these parameters, the three phase traveltime terms control the 'phase', the cosine term in eq. (9) of the sensitivity kernel, while the other terms control the 'amplitude' of the sensitivity kernel. The shape of the sensitivity kernel is determined solely by the phase term such that regions of positive and negative sensitivities are separated by the null lines where the cosine term vanishes.

In this study, we empirically determine the cosine term in eq. (9) and, therefore, the shape of the sensitivity kernel by replacing $\tau_s(\mathbf{x}_r)$ with the phase traveltime measurement for the forward wavefield at the receiver, $\tau_s(\mathbf{x})$ with the forward wavefield's phase traveltime measurements across the USArray, and $\tau_{s^\dagger}(\mathbf{x}, \mathbf{x}_r)$ with the phase traveltime measurements between the receiver to all other location across the USArray using ambient noise cross-correlation measurements. Although the local phase speed can be estimated fairly well through tomographic inversions, such as the isotropic speed maps shown in Fig. 2, and amplitudes can be measured for earthquake events, the amplitude information is typically lost in ambient noise cross correlations due to the time and frequency domain normalizations that are applied during data processing (e.g. Bensen *et al.* 2007). Thus, we will assume that both the forward and adjoint amplitudes are governed by geometrical spreading for a constant speed c_0' reference model (eqs 10b and 10d) and will also assume that $c_0(\mathbf{x}) = c_0' = \frac{|\mathbf{x}_r-\mathbf{x}_e|}{\tau_s(\mathbf{x}_r)-\frac{\pi}{4\omega}}$.

In this case, for $\tau_0 = \frac{|\mathbf{x}_r-\mathbf{x}_e|}{c_0'} = \tau_s(\mathbf{x}_r) - \frac{\pi}{4\omega}$, eq. (9) can be written for an empirical sensitivity kernel as

$$K_{\mathrm{in}}^e\,(\mathbf{x}, \mathbf{x}_r, \omega) = \frac{-2\omega}{|\mathbf{x}_r-\mathbf{x}_e|\,c_0'} \left(\sqrt{\frac{|\mathbf{x}_r-\mathbf{x}_e|}{8\pi k\,|\mathbf{x}-\mathbf{x}_e|\,|\mathbf{x}-\mathbf{x}_r|}}\right) \times \cos\left\{\omega\,[\tau_s\,(\mathbf{x}_r) - \tau_{s^\dagger}\,(\mathbf{x}, \mathbf{x}_r) - \tau_s\,(\mathbf{x})] + \frac{\pi}{2}\right\}. \tag{12}$$

Here again, $k = \frac{\omega}{c'_0}$ but all variables are now measurable quantities. In the presence of strong lateral wave speed variations, focusing and defocusing may affect the amplitude term in eq. (9) significantly, however the phase of kernel (its shape) should continue to be accurate.

Eqs (11) and (12) are analytical and empirical kernels, respectively, at an instantaneous frequency. In practice, phase traveltime measurements at a frequency ω_0 are measured within a finite bandwidth in which a bandpass filter $g(\omega, \omega_0)$ has been applied, so that instantaneous kernels are not entirely appropriate. Considering the linearity of the wave equation, we assume that the event source is modulated by the bandpass filter $g(\omega, \omega_0)$ and the forward wavefield $s(\mathbf{x}, t)$ in eq. (5) can be replaced by

$$s(\mathbf{x}, t) = \int g(\omega, \omega_0) A_s(\mathbf{x}) \cos\{\omega[t - \tau_s(\mathbf{x})]\}\, \mathrm{d}\omega, \tag{13}$$

and the finite bandwidth analytical $K^a_{\mathrm{fb}}(\mathbf{x}, \mathbf{x}_r, \omega_0)$ and empirical $K^e_{\mathrm{fb}}(\mathbf{x}, \mathbf{x}_r, \omega_0)$ sensitivity kernels can be expressed as

$$K^{a,e}_{\mathrm{fb}}(\mathbf{x}, \mathbf{x}_r, \omega_0) = \frac{\int g(\omega, \omega_0)^2 K^{a,e}_{\mathrm{in}}(\mathbf{x}, \mathbf{x}_r, \omega)\, \mathrm{d}\omega}{\int g(\omega, \omega_0)^2 \mathrm{d}\omega}, \tag{14}$$

where $K^a_{\mathrm{in}}(\mathbf{x}, \mathbf{x}_r, \omega)$ and $K^e_{\mathrm{in}}(\mathbf{x}, \mathbf{x}_r, \omega)$ are the analytical and empirical sensitivity kernels for an instantaneous frequency ω given by eqs (11) and (12).

3 METHODS AND RESULTS

We follow closely the ambient noise data processing method described by Lin *et al.* (2008) to obtain the first arriving Rayleigh-wave phase traveltime between each USArray station pair. Although we use traditional frequency–time analysis (FTAN, e.g. Levshin & Ritzwoller 2001; Lin *et al.* 2008) instead of waveform cross correlation to measure the phase traveltime, practically identical results are expected. For each station—referred to as the 'centre station'—all phase traveltime measurements larger than one period between that station and all other stations with a signal-to-noise ratio (SNR) >15 (Bensen *et al.* 2007) are used to determine the phase traveltime map on a $0.2 \times 0.2^\circ$ grid by minimum curvature fitting. Near each centre station, where phase traveltimes are smaller than one period, a linear interpolation is performed by fixing the phase traveltime to $-T/4$ (T is period here) at the centre station location to account the phase shift between force and displacement. We follow the criteria of Lin *et al.* (2009) to select the regions with reliable phase traveltimes. Two examples of 30 s period Rayleigh-wave phase traveltime maps with centre stations G06A and R10A are shown in Figs 3(a) and (b). Note that the $T/4$ phase shift is removed in the phase traveltime maps we plotted such that the traveltime is always zero at the source location. These phase traveltime maps are the basis for the eikonal tomography method presented by Lin *et al.* (2009). The accuracy of the empirical kernel depends on the robustness of the phase traveltime maps. In the presence of large amplitude structural contrasts and strong multipathing (Ji *et al.* 2005; Tape *et al.* 2010), the traveltime maps become less reliable.

To obtain the station–station empirical finite frequency sensitivity kernel for ambient noise applications, the phase traveltime maps for each of the two centre stations are used to measure the parameters in eq. (12). For each field position $\boldsymbol{x}$, we compute the forward phase time $\tau_s(\mathbf{x})$ and adjoint phase time $\tau_{s\dagger}(\mathbf{x}, \mathbf{x}_r)$ from the values of the two phase traveltime maps. Due to the event-receiver symmetry in eq. (12), it is not relevant which station is considered as the event and which station is considered as the receiver.

Fig. 3(c) shows the 30 s instantaneous frequency Rayleigh-wave empirical finite frequency kernel between USArray stations G06A and R10A constructed based on the phase traveltime maps shown in Figs 3(a) and (b). The analytical kernel derived from eq. (11) assuming $c'_0 = \frac{|\mathbf{x}_e - \mathbf{x}_r|}{\tau_s(\mathbf{x}_r) - \frac{\pi}{4\omega}}$ is shown in Fig. 3(d) for comparison. Using c'_0 from the empirical kernel in the analytical kernel minimizes the differences caused by the reference wave speed. In general, the empirical and analytical kernels agree well for this path, which is because of the relatively homogeneous phase velocity distribution between these two stations at this period (Fig. 2b).

Figs 3(e) and (f) show an example of the 30 s finite bandwidth empirical and analytical kernels between stations G06A and R10A. To mimic the bandpassed filter applied in our FTAN analysis, we insert the Gaussian bandpass filter $g(\omega) = e^{-[\frac{4.3(\omega-\omega_0)}{\omega_0}]^2}$ into eq. (14), where ω_0 is the centre frequency of the filter. For simplicity, we assumed no dispersion is present and the phase traveltimes $\tau_s(\mathbf{x}_r)$, $\tau_{s\dagger}(\mathbf{x}, \mathbf{x}_r)$ and $\tau_s(\mathbf{x})$ at 30 s period are used here across the entire frequency band to estimate the instantaneous frequency kernels in eq. (14). Far from the great-circle path, the sensitivity is weaker for the finite bandwidth kernels (Figs 3e and f) than for the instantaneous frequency kernels (Figs 3c and d) due to a destructive interference over the frequency band. The finite bandwidth kernels represent a more realistic sensitivity to the measurement. Although finite bandwidth kernels should be preferred to compute traveltimes or in tomographic inversions, instantaneous frequency kernels do not depend on the specific choice of the bandpass filter and, therefore, are used here in the remainder of this section.

Fig. 4 presents other examples of instantaneous frequency empirical and analytical sensitivity kernels at 20 and 40 s periods for a different station pair, USArray stations L04A and GSL. For this pair of stations there are generally faster phase speeds on the western side of the great-circle path between the stations (Figs 2a and c). East–west phase speed contrasts are, however, stronger at 20 s period than at 40 s. Clear differences are observed between the empirical and analytical sensitivity kernels at 20 s period (Figs 4a and b), where the empirical kernel is not only broader but also is shifted towards the western (faster) side. Kernel cross-sections at the mid-distance from the two stations are shown in Fig. 4(c), in which an east–west asymmetry across the great-circle path is clearly apparent for the empirical sensitivity kernel. The differences between the empirical and analytical kernels can be qualitatively understood by the principle of least-time (or off great-circle propagation effect), in which waves tend to travel through a region with faster phase speed and are, therefore, also more sensitive to it. At 40 s period, the differences between the empirical and analytical kernels (Figs 4d and e) are less pronounced due to the reduced east–west phase speed contrast. Nevertheless, asymmetry can still be observed in the mid-distance cross-section (Fig. 4f). Note that errors in the phase traveltime measurements can generate small-scale distortions in the empirical finite frequency kernels, as irregularities in Figs 4(a) and (d) attest. Only the large-scale features of the empirical kernels are robust.

It is also possible to construct the empirical finite frequency sensitivity kernels within an array for surface waves emitted by an earthquake within or outside the array. The 40 s period Rayleigh wave emitted by a magnitude 6.2 earthquake on 2007 September 6 near Taiwan is used in Fig. 5 as an example of an empirical finite frequency kernel for a teleseismic earthquake. Similar to ambient noise measurements, we first construct the Rayleigh-wave phase traveltime map for the earthquake by using all phase traveltime measurements across the USArray stations (Fig. 5b). To

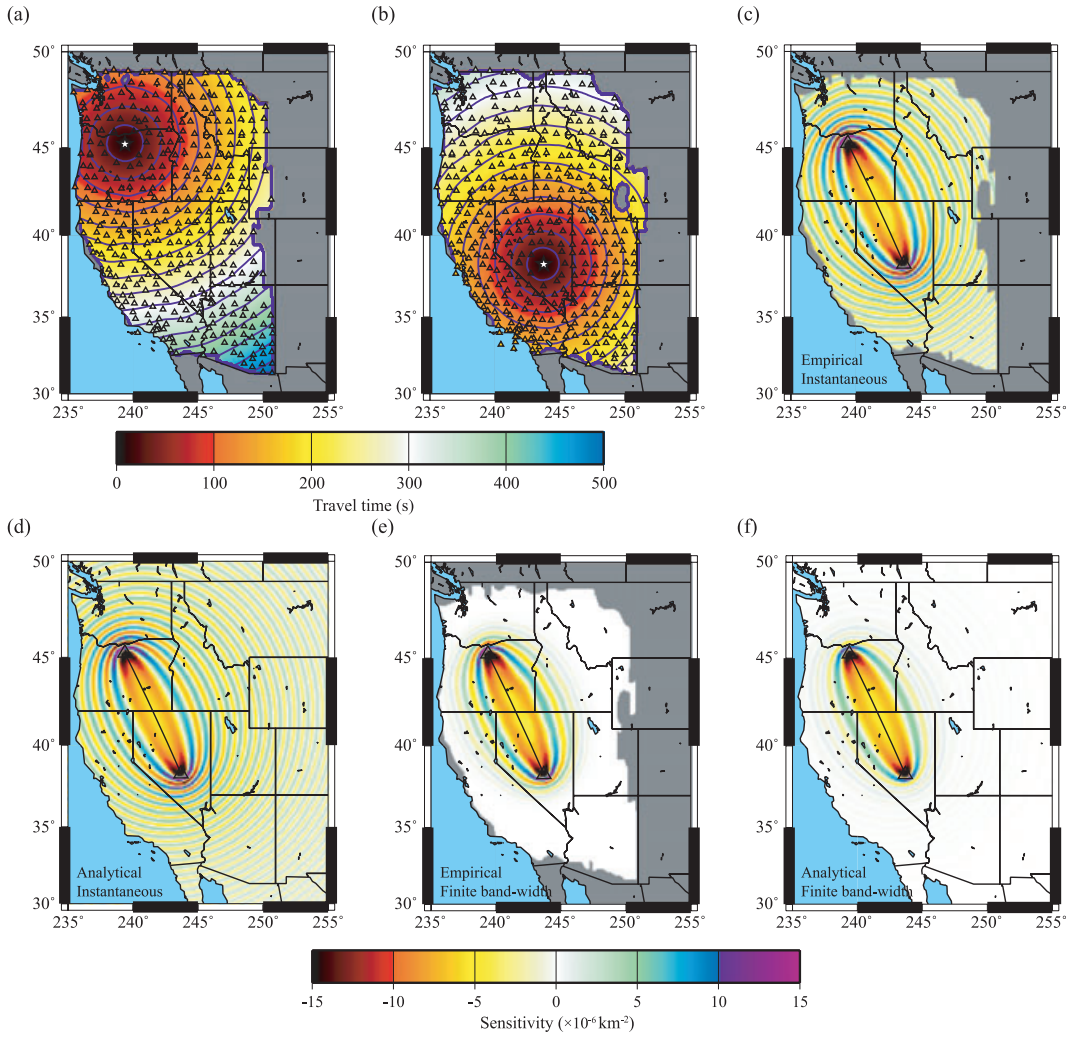

Figure 3. (a) An example 30 s Rayleigh-wave phase traveltime surface for a virtual source located at USArray station G06A (star) based on ambient noise cross correlations. The triangles indicate the stations with good phase traveltime measurements. The blue contours of traveltimes are separated by 30 s. (b) Same as (a), however with USArray station R10A (star) as the virtual source. (c) The 30 s period Rayleigh-wave instantaneous frequency empirical finite frequency kernel for the USArray G06A-R10A station-pair constructed from (a) and (b). The line connecting the two stations is the great-circle path. (d) Same as (c), however with the analytical kernel derived with a constant phase speed reference model. (e) and (f) Same as (c) and (d) however with finite bandwidth empirical and analytical kernels, respectively.

construct the empirical kernel between the earthquake and USArray station X15A within the footprint of the USArray, the 40 s period Rayleigh-wave phase traveltime map for X15A (Fig. 5c) is used to obtain the adjoint phase traveltime $\tau_{s\dagger}(\mathbf{x}, \mathbf{x}_r)$ at each location. For each location, we substitute $\tau_s(\mathbf{x})$ and $\tau_{s\dagger}(\mathbf{x}, \mathbf{x}_r)$ with the values of the forward and adjoint phase traveltime maps, respectively. Although it is possible to measure forward amplitude $A_s(\mathbf{x})$ at each location for earthquakes, we approximate the amplitude by using eq. (10c) for consistency with results from ambient noise.

Fig. 5(d) presents the resulting empirical earthquake-station instantaneous frequency sensitivity kernel and Fig. 5(e) shows the analytical kernel derived from eq. (11), again assuming $c_0 = \frac{|\mathbf{x}_e - \mathbf{x}_r|}{\tau_s(\mathbf{x}_r) - \frac{\pi}{4\omega}}$. The earthquake-station empirical finite frequency kernel across USArray is clearly quite different from the analytical kernel with the centre of the kernel rotated approximately 20° to the south. Due to thin oceanic crust, Rayleigh waves crossing the Pacific at 40 s period have higher phase speeds compared with a global average or with continental areas. The observed Rayleigh wave, therefore, propagates further out into the Pacific basin than predicted by the great-circle ray (Fig. 5a). For earthquakes outside an array the empirical kernels are only determined within the footprint of the array. For earthquakes within an array the earthquake-station empirical kernels would be fully determined.

4 DISCUSSION

One purpose for empirical kernels is to test theoretical kernels constructed either analytically or numerically. Another motivation is to improve predictions of phase traveltimes for surface waves. This is complicated, however, by the fact that the empirical kernels represent partial derivatives computed for the real Earth, $\mathbf{m}_e$, which we do not know. We show here how to use the empirical kernels to compute traveltimes for a model $\mathbf{m}_1$ that is considered to be earth-like ($\mathbf{m}_1 \cong \mathbf{m}_e$), so that $\Delta \boldsymbol{m} = \boldsymbol{m}_1 - \boldsymbol{m}_e$ can be considered to be small. Our suggestion is to construct a hybrid kernel from the empirical kernel and a theoretical kernel based on a reference model $\mathbf{m}_0$, which may be much less earth-like than $\mathbf{m}_1$; that is,

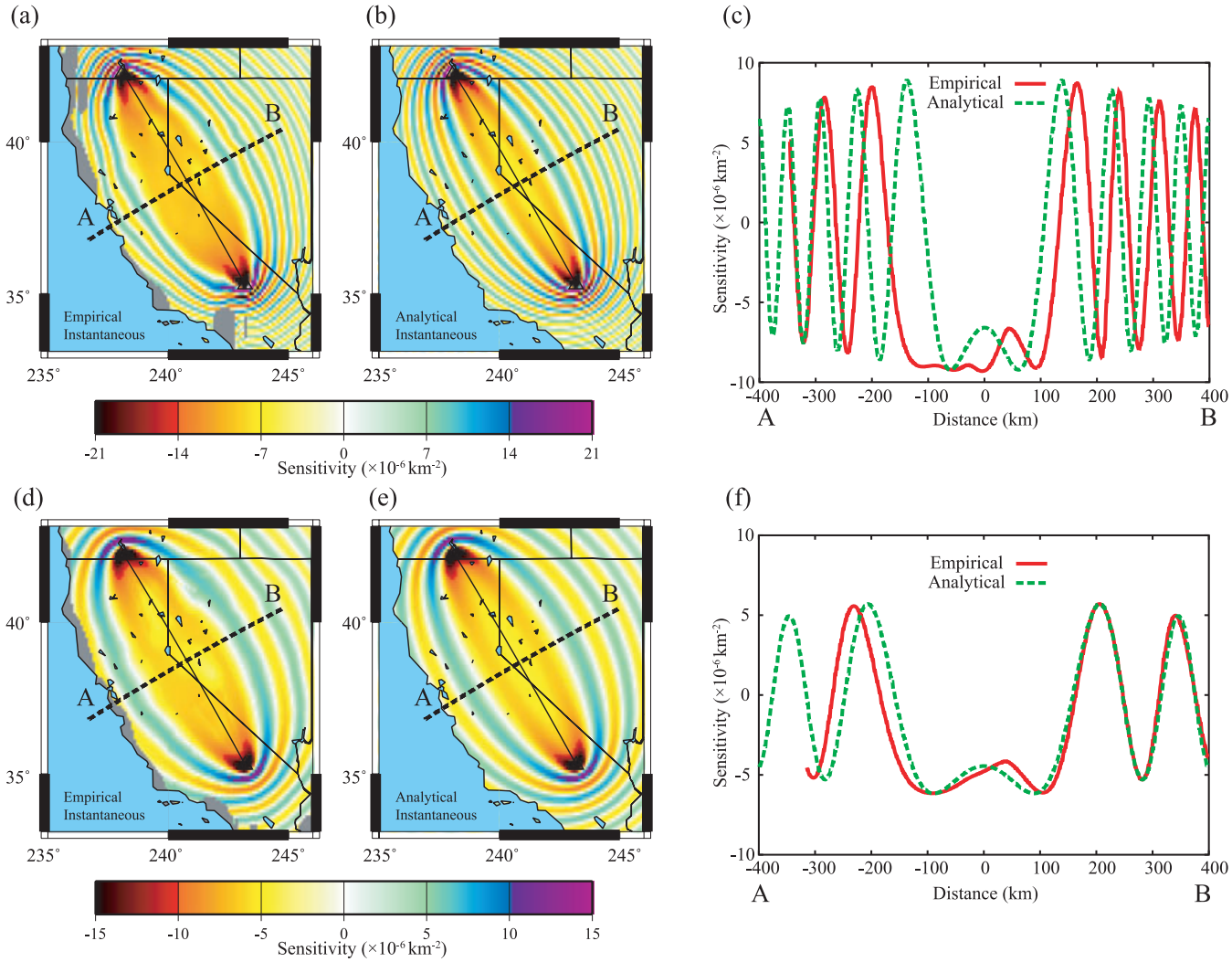

Figure 4. (a) The 20 s period Rayleigh-wave empirical finite frequency kernel for the USArray station pair L04A-GSC. The A-B dashed line indicates the mid-distance cross-section shown in (c). (b) Same as (a), however the analytical kernel is shown. (c) The mid-distance cross-section of the sensitivity kernels shown in (a) and (b). (d)–(f) Same as (a)–(c), however for the 40 s period Rayleigh wave.

$\delta\mathbf{m} = \mathbf{m}_1 - \mathbf{m}_0$ may be much larger than $\Delta\boldsymbol{m}$. In this case, traveltimes computed with the hybrid kernel will be considerably more accurate than those computed using kernels for the reference model.

Consider a reference model $\mathbf{m}_0$ and the real Earth $\mathbf{m}_e$. We seek to predict the traveltime τ for an earth-like model $\mathbf{m}_1$ ($\mathbf{m}_1 \cong \mathbf{m}_e$) that may be significantly different than $\boldsymbol{m}_0$. When the reference model perturbation $\delta\mathbf{m} = \mathbf{m}_1 - \mathbf{m}_0$ is small in some sense, the traveltime for model $\boldsymbol{m}_1$ can be approximated as

$$\begin{aligned}\tau(\mathbf{m}_1) &= \tau(\mathbf{m}_0) + \left.\frac{\partial\tau}{\partial m_i}\right|_{\mathbf{m}_0} \delta m_i + \mathcal{O}\left(\delta\mathbf{m}^2\right) \\ &= \tau(\mathbf{m}_0) + K_i(\mathbf{m}_0)\,\delta m_i + \mathcal{O}\left(\delta\mathbf{m}^2\right),\end{aligned} \tag{15}$$

where, for simplicity of presentation, we have replaced the integral in eq. (1) with a discrete summation over model parameters m_i and have applied Einstein's summation convention. Both the reference traveltime τ_0 and the reference model speed c_0 of eq. (1) have been merged into the kernel K_i here, resulting in a Taylor series expansion of the traveltime function accurate to first order in the model perturbation. When the earth-like model is significantly different than the reference model, the prediction error can be large.

If we expand the traveltime function to include the second-order terms, eq. (15) becomes

$$\begin{aligned}\tau(\mathbf{m}_1) &= \tau(\mathbf{m}_0) + \left.\frac{\partial\tau}{\partial m_i}\right|_{\mathbf{m}_0} \delta m_i + \frac{1}{2}\left.\frac{\partial\tau}{\partial m_i \partial m_j}\right|_{\mathbf{m}_0} \delta m_i \delta m_j + \mathcal{O}\left(\delta\mathbf{m}^3\right) \\ &= \tau(\mathbf{m}_0) + K_i(\mathbf{m}_0)\,\delta m_i + \frac{1}{2}\left.\frac{\partial K_i}{\partial m_j}\right|_{\mathbf{m}_0} \delta m_j \delta m_i + \mathcal{O}\left(\delta\mathbf{m}^3\right).\end{aligned} \tag{16}$$

By substituting

$$\left.\frac{\partial K_i}{\partial m_j}\right|_{\mathbf{m}_0} \delta m_j = K_i(\mathbf{m}_1) - K_i(\mathbf{m}_0) + \mathcal{O}\left(\delta\mathbf{m}^2\right), \tag{17}$$

based on the first-order Taylor expansion of the sensitivity kernel, eq. (16) can be rewritten as

$$\begin{aligned}\tau(\mathbf{m}_1) &= \tau(\mathbf{m}_0) + K_i(\mathbf{m}_0)\,\delta m_i \\ &\quad + \frac{1}{2}\left[K_i(\mathbf{m}_1) - K_i(\mathbf{m}_0)\right]\delta m_i + \mathcal{O}\left(\delta\mathbf{m}^3\right) \\ &= \tau(\mathbf{m}_0) + \frac{1}{2}\left[K_i(\mathbf{m}_1) + K_i(\mathbf{m}_0)\right]\delta m_i + \mathcal{O}\left(\delta\mathbf{m}^3\right),\end{aligned} \tag{18}$$

which yields the traveltime for model $\boldsymbol{m}_1$ accurate to second order in the reference model perturbation. While $K_i(\mathbf{m}_1)$ is generally

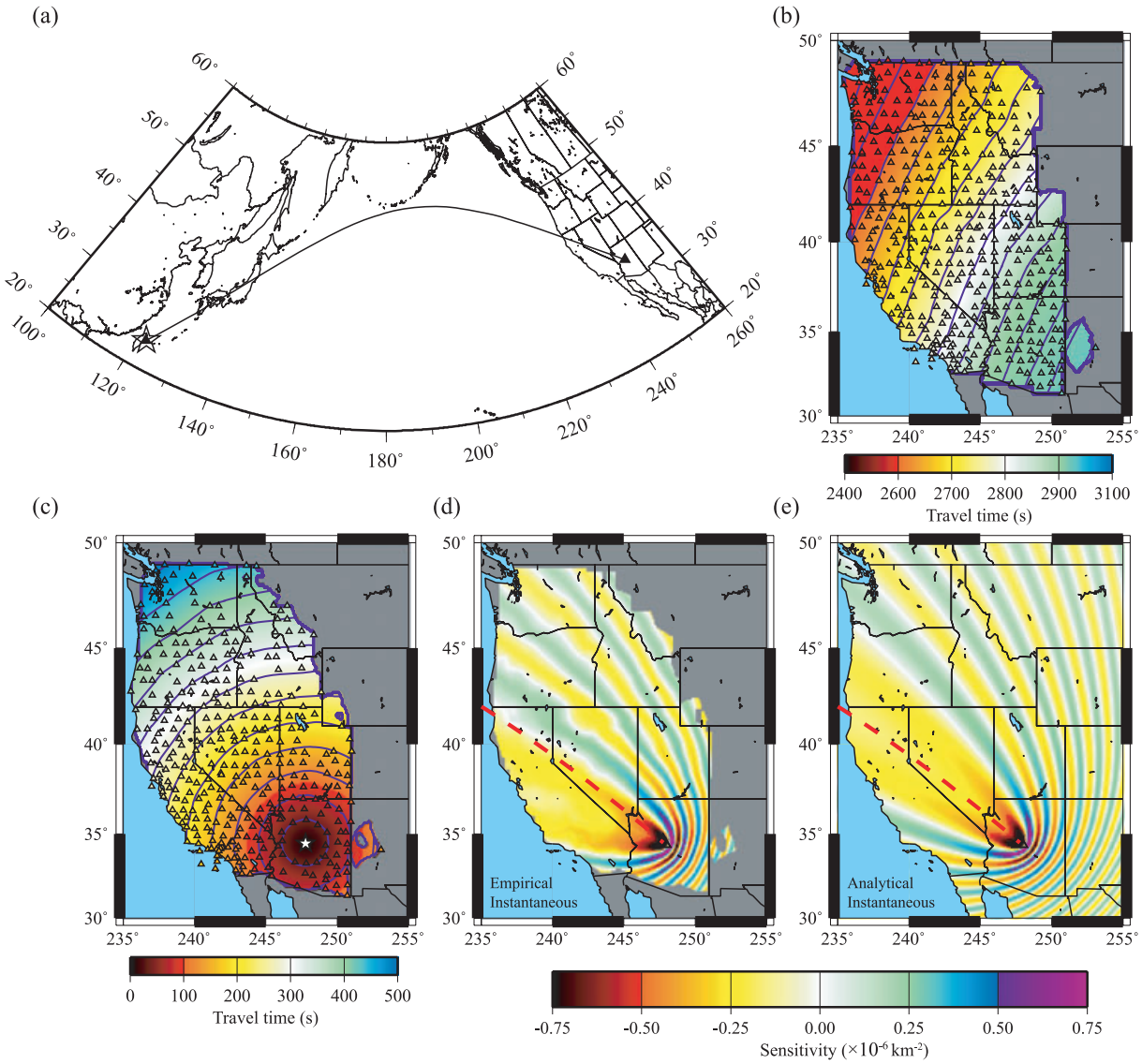

Figure 5. (a) The location of the 2007 September 6 Taiwan earthquake (star), the location of USArray station X15A (triangle) and the great-circle path in between (solid line). (b) The 40 s Rayleigh-wave phase traveltime surface for the Taiwan event shown in (a) observed across the USArray. The triangles indicate the stations deemed to have good phase traveltime measurements. Blue contours of traveltime are separated by 40 s. (c) Same as Fig. 3a, however for 40 s Rayleigh wave with USArray station X15A (star) at the virtual source position. (d) The 40 s period Rayleigh-wave empirical finite frequency kernel for the Taiwan event and USArray station X15A constructed from (b) and (c). The triangle indicates the location of the station and the dashed line indicates the great-circle path between the Taiwan event and the station. (e) Same as (d), however with the analytical kernel derived using a constant phase speed reference model.

unknown without numerical computation, it is possible to approximate $K_i(\mathbf{m}_1)$ by the empirical kernel $K_i(\mathbf{m}_e)$ assuming $\mathbf{m}_1$ is a good representation of the real earth model $\mathbf{m}_e$. In this case, $\Delta\mathbf{m} \equiv \mathbf{m}_1 - \mathbf{m}_e$ will be small and eq. (18) becomes

$$\tau(\mathbf{m}_1) = \tau(\mathbf{m}_0) + \frac{1}{2}\left[K_i(\mathbf{m}_e) + K_i(\mathbf{m}_0)\right]\delta m_i + \left(\frac{1}{2}\left.\frac{\partial K_i}{\partial m_j}\right|_{\mathbf{m}_e}\Delta m_j + \mathcal{O}\left(\Delta\mathbf{m}^2\right)\right)\delta m_i + \mathcal{O}\left(\delta\mathbf{m}^3\right). \quad (19)$$

$$\tau(\mathbf{m}_1) \cong \tau(\mathbf{m}_0) + \frac{1}{2}\left[K_i(\mathbf{m}_e) + K_i(\mathbf{m}_0)\right]\delta m_i + \mathcal{O}(\Delta\mathbf{m}\delta\mathbf{m}) + \mathcal{O}\left(\delta\mathbf{m}^3\right). \quad (20)$$

In eq. (20), the relative size of the error terms is not known exactly. However, if $\boldsymbol{m}_1$ is earth-like, $\Delta\boldsymbol{m}$ will be much smaller than $\delta\boldsymbol{m}$, and the leading order error term will likely be $\mathcal{O}(\delta\mathbf{m}^3)$. Thus, the average of the empirical and reference kernels defines a hybrid empirical kernel, which allows the traveltime to be computed to second-order accuracy for an earth-like model.

To test the application of the hybrid kernel based on eq. (20) to compute traveltimes, we perform a synthetic test to compare a numerically determined phase traveltime with predictions from eqs (15) and (20). A finite difference method is used to solve the 2-D wave equation (Helmholtz equation) to give the 30 s period phase traveltime between two locations separated by 1000 km (triangles in Fig. 6a). Sinusoidal sources are used in all simulations. To emphasize the non-linear relation between traveltime and model perturbations, we assumed an input earth model $\boldsymbol{m}_e$ (Fig. 6a) with a nearly discrete 10 per cent peak-to-peak antisymmetric perturbation relative to the homogeneous reference model $\boldsymbol{m}_0$. Off great-circle

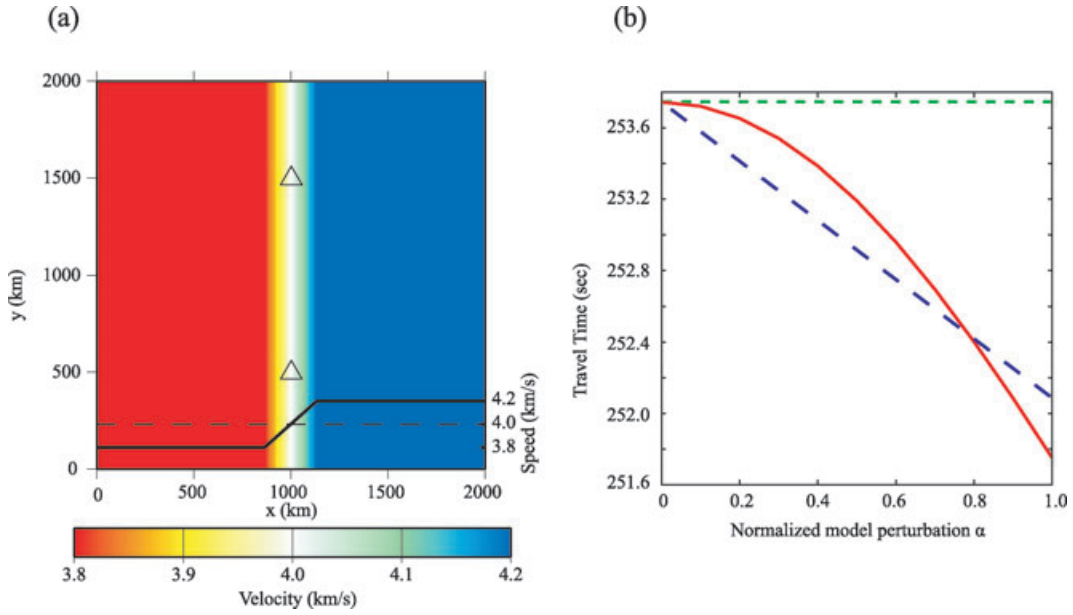

Figure 6. (a) The input earth model $\mathbf{m}_e$ for the synthetic test. The two triangles represent the source or receiver locations in the simulation. A profile through the model is shown as the solid black line where the dashed black line represents the homogeneous reference model $\mathbf{m}_0$. In our simulations, the amplitude of this model is scaled by parameter α that ranges between 0 and 1. (b) The relationship between phase traveltime and model perturbation. The red solid line represents the numerically determined phase traveltime as a function of normalized model perturbation α, the green dashed line is the traveltime based on the analytical kernel, and the blue dashed line is the traveltime from the hybrid empirical kernel.

propagation (a multiscattering phenomenon) is particularly important for waves propagating parallel to the structural boundary, in which case the phase traveltime cannot be predicted accurately by the linear approximation (a single-scattering theory). The symmetry of the analytical kernel $K(\mathbf{m}_0)$ will guarantee a zero traveltime perturbation for the antisymmetric model perturbation.

To demonstrate the non-linearity of the traveltime function, Fig. 6b (red solid line) shows the numerically predicted phase traveltime as a function of model perturbation $\delta\mathbf{m}(\alpha) = \mathbf{m}_1(\alpha) - \mathbf{m}_0 = \alpha(\mathbf{m}_e - \mathbf{m}_0)$, where α is the normalized model perturbation (ranging from 0 to 1) and $\mathbf{m}_1$ is the proposed model (with peak-to-peak structural perturbations ranging from 0 to 10 per cent). The predicted traveltimes using the analytical kernel and eq. (15) are also shown in Fig. 6b (green dashed line). If the proposed model $\mathbf{m}_1$ is near the reference 1-D model $\mathbf{m}_0$, α is small, and the prediction error from the analytical kernel is small. For 5–10 per cent peak-to-peak speed contrasts ($0.5 < \alpha < 1.0$), which ambient noise tomography shows are not atypical in the western United States (Fig. 2), traveltime prediction errors using the analytical kernel can range between 0.5 and 2.0 s, which is not negligible. Such large errors, however, will only result for paths perpendicular to the structural gradient, and average errors for randomly oriented paths will be much smaller. Nevertheless, the paths most sensitive to structural contrasts are also most crucial to resolve sharp boundaries.

To construct the empirical kernel $K(\mathbf{m}_e)$ for the input earth model $\mathbf{m}_e$, we numerically determined the phase traveltime maps centred at the two locations (Figs 7a and b) based on $\mathbf{m}_e$. We follow the method described in previous sections to construct both the finite bandwidth empirical and analytical kernels (Figs 7c and d). The empirical kernel clearly bends towards the faster structure as expected whereas the analytical kernel remains symmetric. Using eq. (20), the predicted traveltimes for different normalized model perturbations α based on the hybrid kernel are shown in Fig. 6(b) (blue dashed line). We note that if the proposed model $\mathbf{m}_1$ is near the reference 1-D model, α is small and $\Delta\mathbf{m}$ is large, and the prediction from the analytical kernel can be better than the hybrid kernel by up to a few tenths of a second. However, when the proposed model $\mathbf{m}_1$ better reflects the earth model $\mathbf{m}_e$ ($\alpha > 0.3$ here), the hybrid kernel will produce more accurate traveltimes than the analytical kernel. When $\mathbf{m}_1 = \mathbf{m}_e$ (or $\alpha = 1$) the hybrid kernel overpredicts the traveltime by about 0.3 s compared with the 2.0 s error resulting from the use of eq. (15). Including the numerically determined synthetic amplitude term in the construction of the empirical kernel does not affect the prediction significantly in this case.

Similar numerical tests, but on a global scale and with a more realistic earth-like reference model, were performed by Peter *et al.* (2009) who numerically determined both the phase traveltime and the sensitivity kernel $K(\mathbf{m}_e)$ for their reference earth model. They showed that for long paths the prediction errors are large using either the analytical kernel $K(\mathbf{m}_o)$ or the numerical kernel $K(\mathbf{m}_e)$ alone with the linear approximation. As shown in their Fig. 3, however, the prediction errors based on the analytical and numerical kernels are anticorrelated. This also suggests that averaging these kernels via eq. (20) will improve the accuracy of the traveltime prediction in a global tomography application.

In principle, for ambient noise tomography the full empirical kernel can be constructed for any interstation path within the array and eq. (20) can be applied. Fig. 8 shows the 30 s Rayleigh-wave phase traveltime misfit as a function of path distance for our straight ray inversion (Barmin *et al.* 2001) with our ambient noise data set in the western United States. The inversion is fully described by Lin *et al.* (2008), however we extend the ambient noise data set here to 2009 September 30. All misfits are summarized by their mean, standard deviation of the mean and standard deviation within each 20 km path distance bin. Positive misfits represent phase traveltime predictions larger (i.e. slower) than the measurements. Both the mean and the standard deviation clearly increase with the path distance. Assuming that the traveltime measurements are equally accurate for short and long paths with similar signal-to-noise characteristics, the increase of the standard deviation of the misfit with

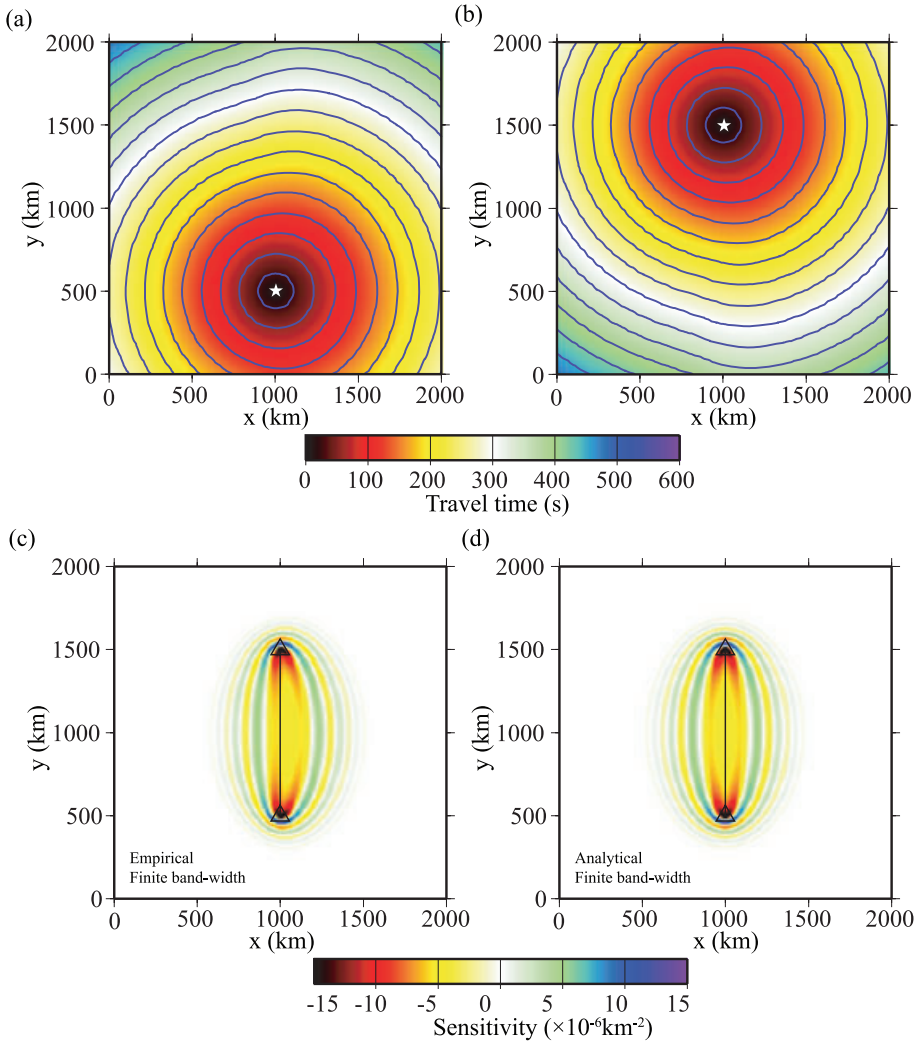

Figure 7. (a) and (b) Synthetic 30 s phase traveltime maps for the two source locations determined by numerical simulation. The blue contours of traveltimes are separated by 30 s. (c) The finite bandwidth empirical kernel between the two triangle locations in Fig. 6(a) constructed with the phase traveltime maps shown in (a) and (b). (d) Same as (c), however with the analytical kernel derived with a constant phase speed reference model.

path distance is probably due to the broader sensitivity kernels for measurements over the longer paths. The systematic overestimation of the traveltime for long paths, however, is probably caused by off great-circle propagation. The eikonal tomography method (Lin *et al.* 2009) accounts for ray bending effects, however prediction of accurate traveltimes remains challenging. We anticipate that the construction of hybrid empirical kernels and the use of eq. (20) will move us beyond both ray theory and single-scattering theory by accounting both for finite frequency and off great-circle effects simultaneously.

5 CONCLUSION

We present a method to construct empirical 2-D finite frequency surface wave sensitivity kernels. We show that by mapping the phase traveltime observed across a large seismic array and utilizing the virtual source property of ambient noise cross-correlation measurements, the adjoint method can be applied to construct empirical sensitivity kernels within the array without numerical simulations. We show that empirical kernels for both ambient noise and earthquake measurements with sources within or outside the array can be constructed within the footprint of the observing array. Because all phase traveltimes are measured via surface waves propagating on the Earth, the empirical kernels represent the sensitivity of surface waves in which the real Earth acts as the reference model.

Significant discrepancies exist between the empirical kernels and analytical kernels derived with a 1-D earth model in regions with large lateral wave speed variations. We show that more accurate traveltime predictions (to second-order in model perturbations) can be achieved by averaging the analytical and empirical kernels than using the analytical kernel alone (first order in model perturbations). Recently, we presented a surface wave tomography method, called eikonal tomography (Lin *et al.* 2009), that measures phase velocities by calculating the gradient of the phase traveltime maps at each spatial location. Although this method accounts for off great-circle propagation, it is still a geometric ray method in principle. We anticipate that both single-scattering (finite frequency effects) and multiscattering effects (off great-circle propagation) can be accounted for simultaneously in a computationally efficient framework with the use of empirical kernels in tomographic inversions. Whether the application of these more accurate finite frequency kernels will produce significant modifications to phase velocity maps and the resulting 3-D models compared to existing ray-theoretic methods (e.g. eikonal tomography) remains to be determined.

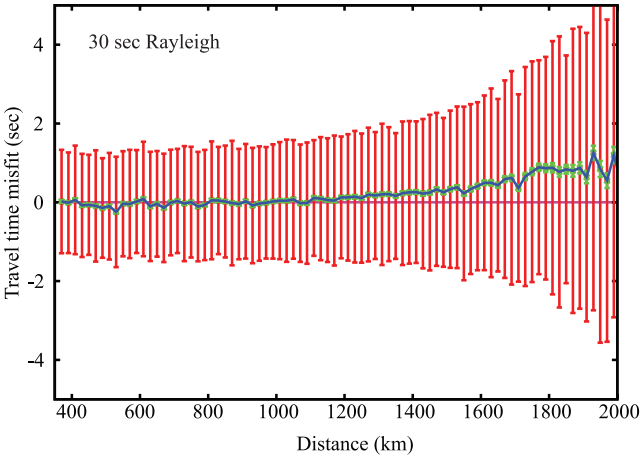

Figure 8. Straight ray inversion misfit for observed (real data) phase traveltimes presented as a function of path distance for 30 s Rayleigh waves in the western United States. All misfits within each 20 km bin are summarized by their mean (blue solid line), standard deviation of the mean (green bars) and standard deviation (red bars). The zero misfit (horizontal solid line) is also shown for reference.

ACKNOWLEDGMENTS

The authors thank Carl Tape and an anonymous reviewer for comments that helped to improve this paper. Instruments (data) used in this study were made available through EarthScope (www.earthscope.org; EAR-0323309), supported by the National Science Foundation. The facilities of the IRIS Data Management System, and specifically the IRIS Data Management Center, were used for access the waveform and metadata required in this study. The IRIS DMS is funded through the National Science Foundation and specifically the GEO Directorate through the Instrumentation and Facilities Program of the National Science Foundation under Cooperative Agreement EAR-0552316. This work has been supported by NSF grants EAR-0711526 and EAR-0844097. F. Lin acknowledges a graduate student scholarship from the SEG Foundation.

REFERENCES

Barmin, M.P., Ritzwoller, M.H. & Levshin, A.L., 2001. A fast and reliable method for surface wave tomography. *Pure appl. Geophys.,* **158**(8), 1351–1375.

Bensen, G.D., Ritzwoller, M.H., Barmin, M.P., Levshin, A.L., Lin, F., Moschetti, M.P., Shapiro, N.M. & Yang, Y., 2007. Processing seismic ambient noise data to obtain reliable broad-band surface wave dispersion measurements. *Geophys. J. Int.,* **169**(3), 1239–1260.

Ji, C., Tsuboi, S., Komatitsch, D. & Tromp, J., 2005. Rayleigh-wave multipathing along the west coast of North America. *Bull. seism. Soc. Am.,* **95**(6), 2115–2124.

Langston, C.A. & Liang, C., 2008. Gradiometry for polarized seismic waves. *J. geophys. Res.,* **113,** B08305, doi:10.1029/2007JB005486.

Levshin, A.L. & Ritzwoller, M.H., 2001. Automated detection, extraction, and measurement of regional surface waves. *Pure appl. Geophys.,* **158**(8), 1531–1545.

Levshin, A.L., Barmin, M.P., Ritzwoller, M.H. & Trampert, J., 2005. Minor-arc and major-arc global surface wave diffraction tomography. *Phys. Earth planet. Inter.,* **149,** 205–223.

Lin, F., Moschetti, M.P. & Ritzwoller, M. H., 2008. Surface wave tomography of the western United States from ambient seismic noise: Rayleigh and Love wave phase velocity maps. *Geophys. J. Int.,* **173**(1), 281–298.

Lin, F., Ritzwoller, M.H. & Snieder, R., 2009. Eikonal tomography: surface wave tomography by phase front tracking across a regional broad-band seismic array. *Geophys. J. Int.,* **177**(3), 1091–1110.

Montelli, R., Nolet, G. & Dahlen, F.A., 2006. Comment on 'Bananadoughnut kernels and mantle tomography' by van der Hilst and de Hoop. *Geophys. J. Int.,* **167,** 1204–1210.

Peter, D., Tape, C., Boschi, L. & Woodhouse, J.H., 2007. Surface wave tomography: global membrane waves and adjoint methods. *Geophys. J. Int.,* **171,** 1098–1117.

Peter, D., Boschi, L. & Woodhouse, J.H., 2009. Tomographic resolution of ray and finite frequency methods: a membrane-wave investigation. *Geophys. J. Int.,* **177,** 624–638.

Pollitz, F.F., 2008. Observations and interpretation of fundamental mode Rayleigh wavefields recorded by the Transportable Array (USArray). *Geophys. J. Int.,* **173,** 189–204.

Ritzwoller, M.H., Shapiro, N.M., Barmin, M.P. & Levshin, A.L., 2002. Global surface wave diffraction tomography. *J. geophys. Res.,* **107**(B12), 2335, doi:10.1029/2002JB001777.

Tanimoto, T., 2008. Normal-mode solution for the seismic noise cross-correlation method. *Geophys. J. Int.,* **175,** 1169–1175.

Tape, C., Liu, Q., Maggi, A. & Tromp, J., 2009. Adjoint tomography of the Southern California crust. *Science.,* **325,** 988–992.

Tape, C., Liu, Q., Maggi, A. & Tromp, J., 2010. Seismic tomography of the southern California crust based on spectral-element and adjoint methods, *Geophys. J. Int.,* **180,** 433–462.

Trampert, J. & Spetzler, J., 2006. Surface wave tomography: finite frequency effects lost in the null space. *Geophys. J. Int.,* **164,** 394–400.

Tromp, J., Tape, C. & Liu, Q., 2005. Seismic tomography, adjoint methods, time reversal and banana-doughnut kernels. *Geophys. J. Int.,* **160,** 195–216.

Van Der Hilst, R.D. & de Hoop, M.V., 2005. Banana-doughnut kernels and mantle tomography. *Geophys. J. Int.,* **163,** 956–961.

Yang, Y.J. & Forsyth D.W., 2006. Regional tomographic inversion of the amplitude and phase of Rayleigh waves with 2-D sensitivity kernels. *Geophys. J. Int.,* **166,** 1148–1160.

Yoshizawa, K. & Kennett, B.L.N., 2002. Determination of the influence zone for surface wave paths. *Geophys. J. Int.,* **149,** 441–454.

Zhou, Y., Dahlen, F.A. & Nolet, G., 2004. Three-dimensional sensitivity kernels for surface wave observables. *Geophys. J. Int.,* **158,** 142–168.